Three-Dimensional Quantum Hall Effect in Topological Amorphous Metals

Jiong-Hao Wang[1] and Yong Xu[1,2*]

1 Center for Quantum Information, IIIS, Tsinghua University, Beijing 100084, People's Republic of China
2 Hefei National Laboratory, Hefei 230088, People's Republic of China
* yongxuphy@tsinghua.edu.cn

Abstract

Weyl semimetals have been theoretically predicted to become topological metals with anomalous Hall conductivity in amorphous systems. However, measuring the anomalous Hall conductivity in realistic materials, particularly those with multiple pairs of Weyl points, is a significant challenge. If a system respects time-reversal symmetry, then the anomalous Hall conductivity even vanishes. As such, it remains an open question how to probe the Weyl band like topology in amorphous materials. Here, we theoretically demonstrate that, under magnetic fields, a topological metal slab in amorphous systems exhibits three-dimensional quantum Hall effect, even in time-reversal invariant systems, thereby providing a feasible approach to exploring Weyl band like topology in amorphous materials. We unveil the topological origin of the quantized Hall conductance by calculating the Bott index. The index is carried by broadened Landau levels with bulk states spatially localized except at critical transition energies. The topological property also results in edge states localized at distinct hinges on two opposite surfaces.

Contents

1   Introduction

Weyl semimetals [1–5], a celebrated example of gapless topological phases, have attracted considerable attention due to both fundamental interest in the emergent Weyl femions as well as novel topological properties and potential applications in future electronic devices [6–34]. Their energy bands touch linearly at a Weyl point protected by the Chern number over a two-dimensional surface enclosing the Weyl point in three-dimensional (3D) momentum space. By bulk-boundary correspondence, topological properties in Weyl semimetals manifest in the surface Fermi arcs connecting Weyl points with opposite chirality, which can give rise to *anomalous* Hall effect [7,8]. Remarkably, such Fermi arc states assisted by bulk chiral Landau levels in Weyl semimetals under magnetic fields can result in 3D quantum Hall effect [35–47].

Apart from crystalline materials with translational symmetry, nature also provides us with abundant amorphous solids without translational symmetry [48]. Although topological physics is established in crystalline materials, recent studies have suggested that amorphous systems can also display various topological phases [49–77] and . In particular, it has been theoretically shown that Weyl semimetals without time-reversal symmetry (TRS) will become topological metals with nonzero anomalous Hall conductivity when lattice sites are positioned randomly [56]. However, it is significantly challenging to experimentally measure the anomalous Hall conductivity in realistic materials, especially for systems with multiple pairs of Weyl points, whose topology can be characterized by the spectral localizer [78–82]. If a system respects TRS, then the anomalous Hall conductivity even vanishes in general. In addition, conventional methods to probe Weyl points and surface states using angle-resolved photoemission spectroscopy (ARPES) [15, 17] may be difficult due to the absence of a well-defined momentum space [see Appendix A for the numerically simulated ARPES spectra]. We therefore ask whether 3D quantum Hall effect can exist in amorphous Weyl materials under magnetic fields, which may provide a feasible approach to probing Weyl band like topology in amorphous materials.

In this work, we theoretically demonstrate that 3D quantum Hall effect can occur in amorphous systems by studying a tight-binding model on a random lattice under a magnetic field [see Fig. 1(a)]. We find the existence of quantized plateaus of the Hall conductance contributed by edge states [see Fig. 1(b)]. The edge states have a topological origin that can be characterized by the Bott index. Despite the presence of strong structural disorder, we show that the bulk states can still form Landau levels, albeit broadened. However, we show that these levels are localized, except at the critical transition point between two plateaus. As a consequence, only edge states contribute to the transport, ultimately resulting in the quantized Hall conductance. In a regular lattice, the 3D quantum Hall effect is explained through semiclassical analysis based on lattice momentum k by showing that electrons cycle along the Fermi arcs on top and bottom surfaces aided by chiral Landau levels tunneling between the opposite surfaces [35,40]. In amorphous systems, while the translational symmetry is entirely lost so that the k space description breaks down, we still observe the edge states localized at distinct hinges on opposite surfaces. We construct a time-reversal invariant model with double pairs of Weyl points when lattice sites are positioned regularly. In both regular and amorphous geometries, it has no *anomalous* Hall conductivity. However, when a magnetic field is applied, we see the appearance of nonzero quantized Hall conductance, demonstrat-
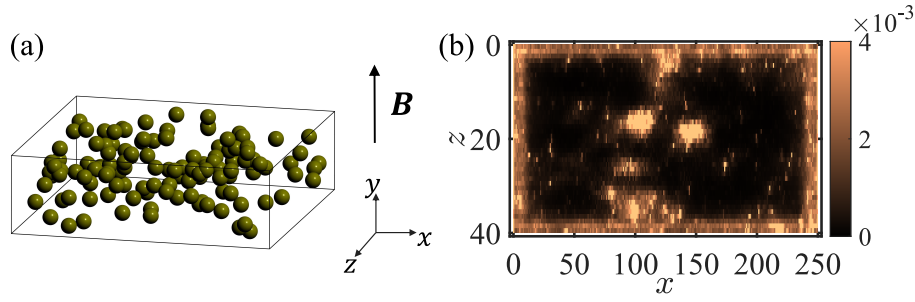
Figure 1: (a) Schematic of a random site configuration in a slab geometry with magnetic fields $\boldsymbol{B}$ along the y direction. (b) Configuration averaged local density of states (DOS) summed over coordinates along y for the Hamiltonian (1) on amorphous lattices with system size $L_x = 250$, $L_y = 20$, and $L_z = 40$ subjected to magnetic fields, illustrating the presence of edge states.

ing that 3D quantum Hall effect can be used as an indicator of topology for amorphous Weyl materials with vanishing *anomalous* Hall conductivity. Finally, we show the three-dimensional quantum Hall effect can also exist under the tilted magnetic field. In this case, we find a region for the time-reversal symmetric model where the quantized Hall conductance is present on amorphous lattices but absent on the regular lattice. The phenomenon is attributed to the additional pair of counter-propagating edge channels on each edge, which are localized on amorphous lattices.

2   Model Hamiltonian

To demonstrate the existence of 3D quantum Hall effect in amorphous systems, we consider the following tight-binding Hamiltonian

$$\hat{H} = \sum_{\boldsymbol{r}} [\hat{c}_{\boldsymbol{r}}^\dagger T_0 \hat{c}_{\boldsymbol{r}} + \sum_{\boldsymbol{d}} t(|\boldsymbol{d}|)\hat{c}_{\boldsymbol{r}+\boldsymbol{d}}^\dagger T(\hat{\boldsymbol{d}})\hat{c}_{\boldsymbol{r}}], \tag{1}$$

where $\hat{c}_{\boldsymbol{r}}^\dagger = (\hat{c}_{\boldsymbol{r},\uparrow}^\dagger, \hat{c}_{\boldsymbol{r},\downarrow}^\dagger)$ with $\hat{c}_{\boldsymbol{r},\sigma}^\dagger$ being the fermionic creation operator of spin σ at position $\boldsymbol{r}$, and $\hat{c}_{\boldsymbol{r}}$ being its Hermitian conjugate, the corresponding annihilation operator. $T_0 = M(k_w^2-6)$ $\sigma_z+(4D_2+2D_1)\sigma_0$ is the onsite term, and $T(\hat{\boldsymbol{d}}) = M\sigma_z+i(\gamma/2)(\hat{d}_x\sigma_x+\hat{d}_y\sigma_y)-(D_2\hat{d}_x^2+D_1\hat{d}_y^2+D_2\hat{d}_z^2)\sigma_0$ is the hopping matrix from the site at position $\boldsymbol{r}$ to a different site at $\boldsymbol{r}+\boldsymbol{d}$, where σ_0 is the identity matrix, σ_ν ($\nu=x,y,z$) are Pauli matrices, and $\hat{\boldsymbol{d}} = \boldsymbol{d}/|\boldsymbol{d}| = (\hat{d}_x, \hat{d}_y, \hat{d}_z)$ is the normalized separation vector. In the amorphous case, we set $t(|\boldsymbol{d}|) = \Theta(R_c - |\boldsymbol{d}|)e^{-\lambda(|\boldsymbol{d}|/a-1)}$, decaying exponentially to simulate real materials. Here, $\Theta(R_c-|\boldsymbol{d}|)$ is the Heaviside step function such that hoppings for $|\boldsymbol{d}| > R_c$ are cut off and the lattice constant is set to $a = 1$. In a regular lattice with only nearest-neighbor hopping, i.e. the hopping strength $t(|\boldsymbol{d}|)$ set to be 1 for nearest neighbor and 0 otherwise, the Hamiltonian (1) reduces to a paradigmatic Weyl semimetal model corresponding to a momentum space Hamiltonian $H(\boldsymbol{k}) = M(k_w^2-\boldsymbol{k}^2)\sigma_z+\gamma(k_x\sigma_x+k_y\sigma_y) + D_1k_y^2 + D_2(k_x^2 + k_z^2)$ in the continuum limit, where M, k_w, γ, D_1 and D_2 are real system parameters. The Weyl points are located at $\boldsymbol{k} = (0,0,\pm k_w)$ with energy $E_w = D_2 k_w^2$. When $D_1, D_2 \neq 0$, Fermi arcs are bent, which is essential to 3D quantum Hall effect when the Fermi energy lies at the energy of Weyl points [35,40].

In the amorphous case, we consider sites that are positioned completely randomly in a slab, which is thin along y, necessary to the observation of quantum Hall effect even in the pristine regular topological semimetal [see Appendix B]. To be explicit, the positions of lattice
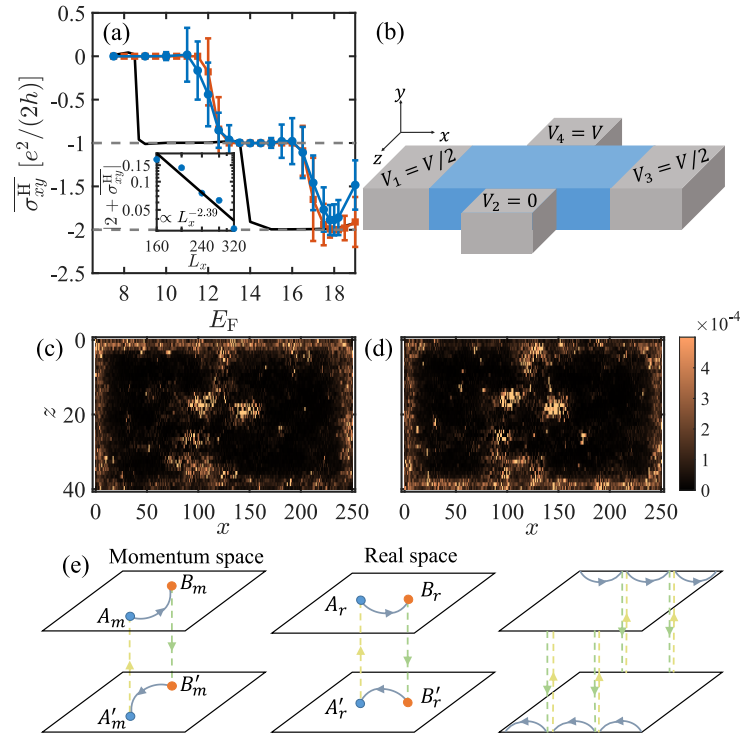
Figure 2: (a) Sample averaged Hall conductance $\overline{\sigma^{\mathrm{H}}_{xy}}$ (blue line) and Bott index (red line) versus the Fermi energy E_{F} of the Hamiltonian (1) under magnetic fields on amorphous lattices compared with the Hall conductance on regular lattices (black line). The system size for the Hall conductance is $L_x = 200, L_y = 20, L_z = 40$ and that for the Bott index is $L_x = 25, L_y = 20, L_z = 44$. Inset: the Hall conductance at $E_{\mathrm{F}} = 18.2$ for $L_x = 160, 200, 240, 280, 320$ (blue points) fitted by a black line in the logarithmic scale, exhibiting the power-law decay. We keep the ratio $L_x/L_z = 5$, and $L_y = 20$ is fixed. (b) Schematic illustration of a four-terminal setup to extract the Hall conductance. (c-d) Sample averaged local DOS on the top and bottom layer, respectively, calculated for $L_x = 250, L_y = 20, L_z = 40$ within $L_y - 1 \leq z \leq L_y$ and $0 \leq z \leq 1$ (e) Schematic of cyclic trajectories of an electron under magnetic fields [in momentum space (left panel) and real space (middle panel)] and the resulting skipping edge states (right panel).

sites are sampled from uncorrelated uniform distributions within the interval $[0, L_\nu)$, where L_ν is the length of the system along ν with $\nu = x, y, z$. We take the total number of sites as $N = \rho V$ with the volume of the system $V = L_x L_y L_z$ and the average density $\rho = 1$. An external magnetic field $\boldsymbol{B} = (0, B, 0)$ is applied in the y direction [see Fig. 1(a)]. The magnetic field modifies the hopping matrix $T(\hat{\boldsymbol{d}})$ by a phase factor $e^{-i\frac{e}{\hbar} \int_r^{r+d} \boldsymbol{A} \cdot d\boldsymbol{r}'}$ where the physical constants are set to be $e = \hbar = 1$ and we choose a gauge such that the vector potential is $\boldsymbol{A} = (Bz, 0, 0)$. Note that without changing the physics qualitatively, we follow previous works to ignore the contribution of the Zeeman effect [35, 40]. In numerical computations throughout the paper, we take $M = 8, \gamma = 50, k_w = 1.5, D_1 = 1, D_2 = 4, R_c = 2.5, B = \pi/22$ and $\lambda = 3$ without loss of generality, and the results are averaged over 100 sample configurations unless stated otherwise.

In a regular lattice, the Hamiltonian (1) hosts Fermi arcs on top and bottom surfaces viewed in the y direction. The Fermi arcs contribute to edge channels with the assistance of bulk chiral Landau levels under magnetic fields, giving rise to 3D quantum Hall effect [35, 40]. In

the amorphous case, while previous study suggests the existence of surface states despite the absence of translational symmetry [56], it is unclear whether isolated Landau levels can survive so as to result in 3D quantum Hall effect. To investigate the possibility, we will calculate the Hall conductance, the Bott index, the DOS and the localization properties of the Hamiltonian (1) in random site configurations.

3 Hall conductance, Bott index and edge states

To show the presence of 3D quantum Hall effect in amorphous systems, we calculate the Hall conductance using Landauer-Büttiker formula under four-terminal measurement with voltage $V_1 = V_3 = V/2, V_4 = V$ and $V_2 = 0$ applied on ideal leads, as shown in Fig. 2(b). Note that the terminal configuration here is different from that for measuring anomalous Hall effect, e.g., in Ref. [56], with the surfaces connected to terminal 2 and 4 carrying no Fermi arcs. The Hall conductance σ_{xy}^{H} is given by [56]

$$\sigma_{xy}^{\mathrm{H}} = \frac{e^2}{2h}(T_{14} - T_{12}),\tag{2}$$

where T_{ij} is the transmission probability from lead j to i computed numerically using non-equilibrium Green's function method [83–86]. In the phase with 3D quantum Hall effect, σ_{xy}^{H} is quantized to an integer multiple of $e^2/(2h)$. Note that in the quantized region, the Hall conductance determined by Eq. (2) is identical to that measured under constant longitudinal and no transverse current up to a multiplier $1/2$ [35, 40].

In Fig. 2(a), we plot the sample averaged Hall conductance $\overline{\sigma_{xy}^{\mathrm{H}}}$ with respect to the Fermi energy E_{F} (blue line). Remarkably, we see a plateau quantized at $\overline{\sigma_{xy}^{\mathrm{H}}} = -e^2/(2h)$ in the region $13 \lesssim E_{\mathrm{F}} \lesssim 16$, establishing the presence of amorphous 3D quantum Hall effect. Specifically, as E_{F} is increased from $E_{\mathrm{F}} = 7.5$, we see $\overline{\sigma_{xy}^{\mathrm{H}}} = 0$ for $E_{\mathrm{F}} \lesssim 11$ and then $\overline{\sigma_{xy}^{\mathrm{H}}}$ undergoes a transition around $E_{\mathrm{F}} \approx 12$ into the plateau at $\overline{\sigma_{xy}^{\mathrm{H}}} = -e^2/(2h)$. As we further raise E_{F}, $\overline{\sigma_{xy}^{\mathrm{H}}}$ declines and reaches a plateau near $\overline{\sigma_{xy}^{\mathrm{H}}} = -2e^2/(2h)$ for $17.8 \lesssim E_{\mathrm{F}} \lesssim 18.2$. Our numerical calculations further show that $|2 + \overline{\sigma_{xy}^{\mathrm{H}}}| \propto L_x^{-2.39}$ with system size L_x at $E_{\mathrm{F}} = 18.2$ [see the inset of Fig. 2(a)], suggesting that within this region, $\overline{\sigma_{xy}^{\mathrm{H}}}$ can reach the quantized value of $-2e^2/(2h)$ in the thermodynamic limit. Compared with the Hall conductance $\overline{\sigma_{xy}^{\mathrm{H}}}$ of a system with regular lattice sites (black line), we see that the corresponding plateaus for the amorphous system move toward higher E_{F}, which is attributed to the shift of Landau levels in the amorphous case as will be discussed later.

To reveal the topological nature of 3D quantum Hall effect, we calculate the Bott index [87, 88] defined as

$$\mathrm{Bott} = \frac{1}{2\pi}\mathrm{ImTr}\log(U_z U_x U_z^\dagger U_x^\dagger),\tag{3}$$

where $[U_\nu]_{mn} = \langle\psi_m|e^{i2\pi\hat{\nu}/L_\nu}|\psi_n\rangle$ ($\nu = z, x$) with $\hat{\nu}$ being position operators along ν and $|\psi_n\rangle$ $(1, 2, ..., N_{occ})$ being occupied single-particle states under E_{F}. In our numerical computations, we impose periodic boundary conditions (PBCs) along x and z and open boundary conditions (OBCs) along y, given the fact that the surface states on top and bottom surfaces are crucial to the 3D quantum Hall effect.

Figure 2(a) shows the computed Bott index (red line), which agrees well with the Hall conductance (blue line). In fact, the Bott index is less affected by finite-size effects due to the imposed PBCs. To be specific, for $17.8 \lesssim E_{\mathrm{F}} \lesssim 18.2$, the Bott index is well quantized at

Bott $= -2$, further verifying the existence of the plateau with $\overline{\sigma_{xy}^{H}} = -2e^2/(2h)$ in thermo-dynamic limit. In addition, within the transition region between quantized plateaus, the Bott index exhibits a sharper decline than the Hall conductance. The consistence between the Bott index and the Hall conductance thus establishes the topological origin of the 3D quantum Hall effect.

Because of the topological properties, we expect the existence of hinge states on top and bottom surfaces, leading to the 3D quantum Hall effect. To identify the hinge states, we calculate the local DOS at energy E and position r based on

$$\rho(r, E) = -\frac{1}{\pi} \text{ImTr} \, G_{rr}(E) \tag{4}$$

using the recursive Green's function method [83, 84]. Here, $G_{rr}(E) = \langle r | (E - H + i0^+)^{-1} | r \rangle$ where H is the single-particle first quantization form of the Hamiltonian (1) under OBCs along all three directions, 0^+ denotes a positive infinitesimal, and $|r\rangle$ is the site state at position r. Figure 1(b) shows the local DOS at $E = 14$ summed over the coordinates along y, remarkably exhibiting the existence of edge states despite the presence of strong structural disorder. Note that the small bright regions in the interior are contributed by localized bulk states (here the bulk states refer to the states calculated under OBCs along y and PBCs along x and z and edge states can only be obtained by further applying OBCs along either x or z or both) due to the finite number of samples. Ref. [56] shows that a Weyl semimetal develops into a topological metal in a random lattice with surface states. Such edge states on top and bottom surfaces thus arise from these surface states under magnetic fields.

Figure 2(c) and (d) further display the local DOS at the top and bottom layer along y, respectively. It surprisingly illustrates that the hinge states are primarily concentrated at the $z = 0$ edge on the top surface [Fig. 2(c)] while at the other edge on the bottom surface [Fig. 2(d)]. In a regular lattice, such a distribution of hinge states on opposite surfaces arises from Fermi arc states assisted by bulk chiral Landau levels [35, 40]. Specifically, according to the semiclassical equations of motion, $\dot{r} = \partial \varepsilon_k/(\hbar \partial k)$ and $\hbar \dot{k} = -e\dot{r} \times B$ [89], if an electron starts at A_m in momentum space and A_r in real space, then under magnetic fields, it will move from A_m to B_m in momentum space following the Fermi arc. Meanwhile, the electron moves from A_r to B_r in real space [see Fig. 2(e)]. At B_m, the electron tunnels to B'_m on the opposite surface through a bulk chiral Landau level. In real space, the electron tunnels to B'_r on the opposite surface. On the bottom surface, the electron further moves from B'_m (B'_r) to A'_m (A'_r) in momentum (real) space, completing cyclic motions in both momentum and real spaces. Such cyclic motions form Landau levels. However, at the edges of the top and bottom surfaces, such cyclic motions are not allowed, leading to skipping edge states. While the semiclassical analysis is based on k space for translational-invariant systems, our results show the presence of the distinct profile of the local DOS for edge states on opposite surfaces in amorphous systems.

4 Landau levels and localization properties

To further elaborate on the mechanism of 3D quantum Hall effect, we compute the DOS defined as $\rho(E) = \sum_i \delta(E - E_i)/(2N)$, where E_i is the ith eigenvalue of the Hamiltonian and $N = L_x L_y L_z$. We use the kernel polynomial method (KPM) to compute the DOS with Chebyshev expansion up to order N_c [90] under the same boundary conditions as for the Bott index. To study the localization properties, we calculate the localization length of the system in a long bar geometry [91, 92] by

$$\lambda^{-1}(E) = -\lim_{L_z \to \infty} \frac{1}{2L_z} \log \text{Tr}\,[G_{1z}(E) G_{1z}^{\dagger}(E)], \tag{5}$$
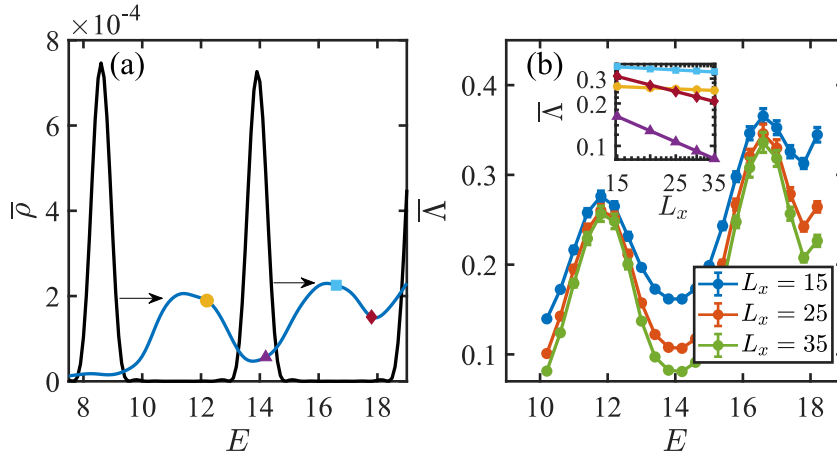
Figure 3: (a) Sample averaged DOS $\overline{\rho}(E)$ versus the energy E for amorphous systems (blue line) and regular lattices (black line), computed by the KPM with the expansion order $N_c = 2^{13}$. Here, $L_x = 25$, $L_y = 20$, and $L_z = 44$. Arrows indicate the shifting direction of Landau levels induced by structural disorder. (b) Sample averaged normalized localization length $\overline{\Lambda}$ with respect to E for $L_x = 15, 25$ and 35. Here $L_y = 20$ and $L_z = 10^4$. The inset shows the finite-size scaling of $\overline{\Lambda}$ versus L_x at $E = 12.2$, 14.2, 16.6 and 17.8 [highlighted by yellow circle, purple triangle, blue square and red diamond in (a), respectively]. For $E = 14.2$ and 17.8, we take $L_z = 10^4$ and $L_y = 20$, and for $E = 12.2$ and 16.6, we take $L_z = 10^5$ and $L_y = 20$ (the results are averaged over 40 samples).

where $G_{1z}(E) = \langle 1|(E - H + i0^+)^{-1}|z\rangle$ is the submatrix of the Green's function between the site states in the first and final layer along z, which can be obtained iteratively after partitioning the bar into layers each with thickness R_c along z [83,84]. In the calculations, we apply PBCs along x and OBCs along y and z.

Figure 3(a) displays the sample averaged DOS $\overline{\rho}(E)$ as a function of energy E (blue line), remarkably showing the existence of Landau levels despite the presence of strong structural disorder in amorphous lattices. In stark contrast to the regular case (black line), the Landau levels are broadened, resulting in an overlap between neighboring levels. The system thus cannot form band insulators for the bulk states as in the regular case. Fortunately, these states are spatially localized as reflected by the decrease of the averaged normalized localization length $\overline{\Lambda} = \overline{\lambda}/L_x$ with the increasing of system sizes [see Fig. 3(b)] [91,92]. Since the localized states have no contribution to electrical transport, the quantized Hall conductance is attributed to the edge states (see the following discussion). Figure 3(b) also suggests that around the peaks of the two Landau levels, $\overline{\Lambda}$ converges to finite values as the system enlarges, signaling critical extended behaviors. Such critical points correspond to the transition points between neighboring plateaus of the Hall conductance. Specifically, we fit $\overline{\Lambda}$ computed for different system sizes as $\overline{\Lambda} \propto L_x^{-\alpha}$ at $E = 12.2$ (yellow circle), 14.2 (purple triangle), 16.6 (blue square) and 17.8 (red diamond), yielding $\alpha = 0.07, 0.82, 0.09$ and 0.48, respectively [see the inset of Fig. 3(b)]. The nonzero slope α suggests the localized character. For $E = 12.2$ and 16.6, the slope α is very small, indicating their closeness to critical energies. Note that the critical energies are difficult to determine accurately in our 3D case due to the large consumption of computational resources. This mechanism of the broadening of Landau levels and localization of bulk states is generic, implying that 3D quantum Hall effect can be observed as long as the Landau levels are not too close in the energy space, independent of the details of the model.

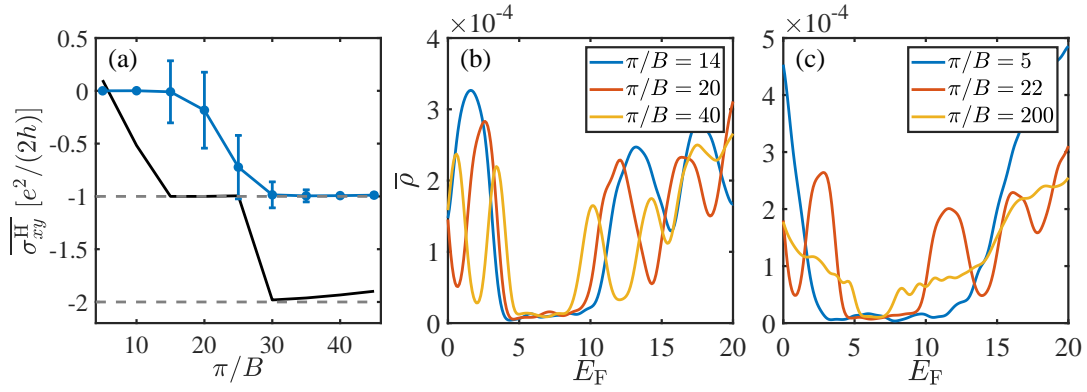Figure 3(a) also illustrates that the Landau levels in our amorphous lattices move to higher

Figure 4: (a) Sample averaged Hall conductance $\overline{\sigma_{xy}^{\mathrm{H}}}$ with respect to the inverse of the magnetic field B at $E_{\mathrm{F}} = 12$ for the regular lattice (black line) with $L_x = 300, L_y = 20, L_z = 40$ and amorphous lattices (blue line) with $L_x = 200, L_y = 20, L_z = 40$. (b-c) Sample averaged DOS calculated under various magnitudes of the magnetic field.

energy compared with its regular counterpart (black line), explaining the up-moving behavior of the Hall conductance plateau mentioned above .

5 Effect of the magnitude of the magnetic field

To elaborate on the effect of the magnitude of the magnetic field on the 3D quantum Hall effect, we calculate the sample averaged Hall conductance $\overline{\sigma_{xy}^{\mathrm{H}}}$ with respect to the inverse of the magnetic field B at a fixed E_{F}, as shown in Fig. 4(a). We see quantized plateaus in both regular (black line) and amorphous lattices (blue line) and as the magnitude of the magnetic field decreases (π/B increases), the Hall conductance transitions from one plateau to another one with larger absolute value. The transition is attributed to the shifting of the Landau levels to lower energy as the magnetic field decreases, as shown in Fig. 4(b) for amorphous lattices. We also observe that the plateaus of the Hall conductance on amorphous lattices float upwards compared with the regular lattice, which is caused by the right moving of the Landau levels in the energy space induced by the structural disorder as we have explained in Fig. 3(a).

The magnitude of the magnetic field cannot be too small for the occurrence of 3D quantum Hall effect which can be understood easily by taking the limit of no magnetic field under which no quantum Hall effect arises. When the magnetic field is too large, the 3D quantum Hall effect will also disappear. Intuitively, as the strength of the magnetic field increases, the bulk states with energy further away from the Weyl points will be squeezed into Landau levels together with the Fermi arc states near the Weyl points, because the degeneracy of the Landau level is proportional to the magnitude of the magnetic field. Away from the Weyl points, the bulk DOS is large, reminiscent of the conventional 3D metal, leading to the disappearance of well-separated Landau levels even on the regular lattice. Thus, the magnitude of the magnetic field has an upper bound for the 3D quantum Hall effect. To justify our arguments above, we calculate the DOS on amorphous lattices as shown in Fig. 4(c) under magnetic fields with magnitude $\pi/B = 5, 22$ and 200. Only for moderate magnitude $\pi/B = 22$ (the red line), we see clear patterns of broadened Landau levels with stark contrast between peaks and valleys, which often implies the existence of quantum Hall effect. Under too large (the blue line) and too tiny (the yellow line) magnetic field, Landau levels cannot be identified, indicating the absence of quantum Hall effect. Therefore, the occurrence of 3D quantum Hall effect requires
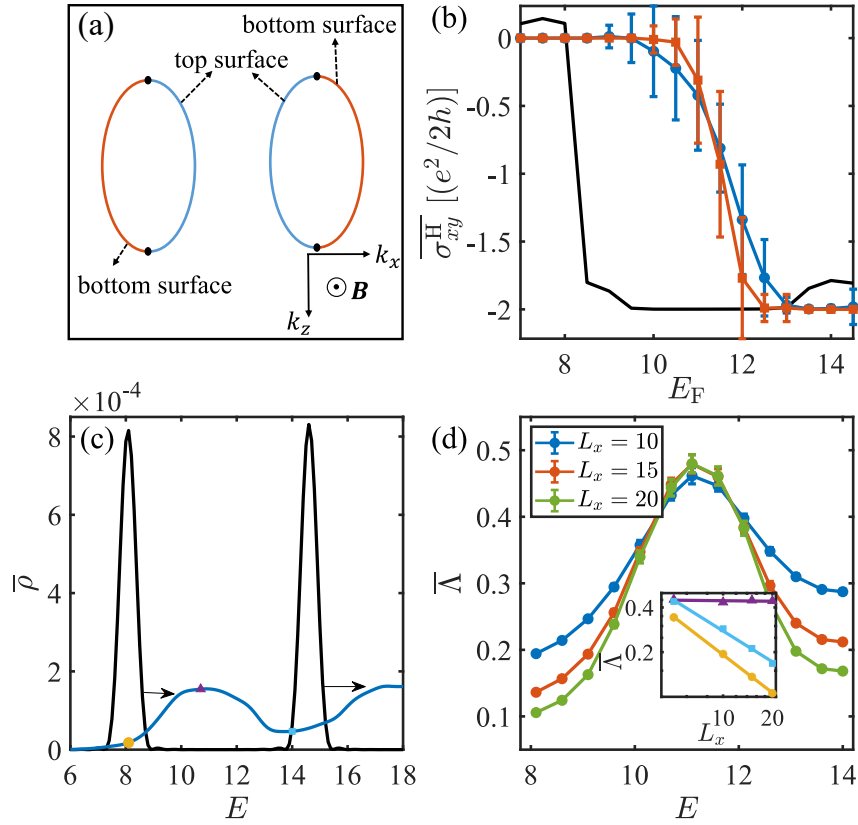
Figure 5: (a) Schematic of the Weyl points and Fermi arcs for the Hamiltonian (6) with TRS on regular lattices. (b) Configuration averaged Hall conductance versus the Fermi energy for the Hamiltonian (6) on amorphous (blue line) and regular (black line) lattices. Th red line shows the Bott index on amorphous lattices. (c) Sample averaged DOS versus the energy E for amorphous systems (blue line) and regular lattices (black line). (d) Normalized localization length $\bar{\Lambda}$ averaged over 40 samples with respect to E with $L_y = 20$ and $L_z = 10^4$. The inset shows the finite-size scaling of $\bar{\Lambda}$ versus L_x at $E = 8.1, 10.7$ and 14 [highlighted by yellow circle, purple triangle and cyan square in (c), respectively].

the magnetic field in a moderate range of magnitude.

6   Model with TRS

To demonstrate that 3D quantum Hall effect can be utilized to detect the Weyl band like topological properties in amorphous systems with TRS, we construct the following Hamiltonian,

$$\hat{H}_T = \sum_{\boldsymbol{r}} [\hat{c}_{\boldsymbol{r}}^{\dagger} T_T^0 \hat{c}_{\boldsymbol{r}} + \sum_{\boldsymbol{d}} t(|\boldsymbol{d}|)\hat{c}_{\boldsymbol{r}+\boldsymbol{d}}^{\dagger} T_T(\hat{\boldsymbol{d}})\hat{c}_{\boldsymbol{r}}] \tag{6}$$

with four internal degrees of freedom at each site, i.e. $\hat{c}_{\boldsymbol{r}}^{\dagger} = (\hat{c}_{\boldsymbol{r},1}^{\dagger}, \hat{c}_{\boldsymbol{r},2}^{\dagger}, \hat{c}_{\boldsymbol{r},3}^{\dagger}, \hat{c}_{\boldsymbol{r},4}^{\dagger})$. Here $T_T^0 = M(k_w^2 -6)\tau_z\sigma_0 + (4D_2 + 2D_1)\tau_0\sigma_0 + \beta\tau_y\sigma_y$ and $T_T(\hat{\boldsymbol{d}}) = M\tau_z\sigma_0 + (i\gamma/2)(\hat{d}_x\tau_x\sigma_z + \hat{d}_y\tau_y\sigma_0) - (D_2\hat{d}_x^2 + D_1\hat{d}_y^2 + D_2\hat{d}_z^2)\tau_0\sigma_0 + i\alpha\hat{d}_y\tau_x\sigma_y/2$, with τ_x ($\nu = x, y, z$) being another set of Pauli matrices referring to orbital degrees of freedom. The Hamiltonian respects TRS, i.e. $\hat{T}\hat{H}_T\hat{T}^{-1} = \hat{H}_T$ with time-reversal operator $\hat{T}$ acting as $\hat{T}i\hat{T}^{-1} = -i$ and $\hat{T}\hat{c}_{\boldsymbol{r}}\hat{T}^{-1} = i\tau_0\sigma_y\hat{c}_{\boldsymbol{r}}$. In this section, we take $M = 13, \alpha = -80, \beta = 20, B = \pi/22$ and other parameters the same as before.

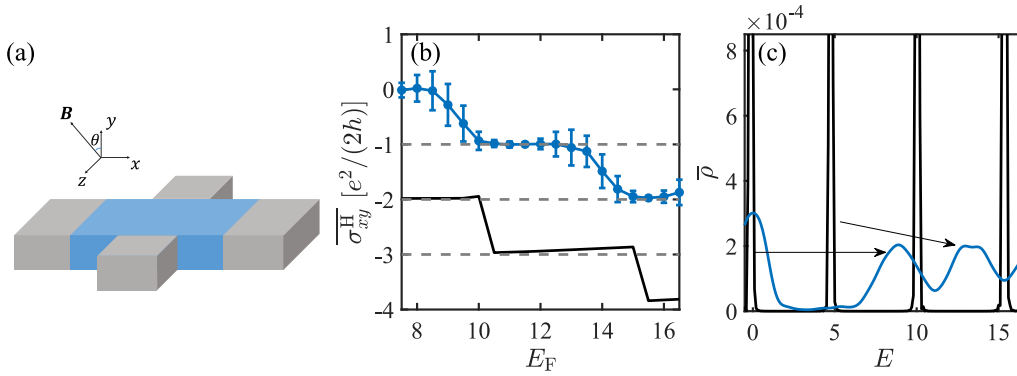Figure 6: (a) Schematic of the sample under a tilted magnetic field **B**. (b) Configuration averaged Hall conductance $\overline{\sigma^{\mathrm{H}}_{xy}}$ with respect to the Fermi energy E_{F} for the Hamiltonian (1) on amorphous (the blue line) and regular (the black line) lattices. The sample size is $L_x = 200, L_y = 20, L_z = 40$ and the parameters of the Hamiltonian are the same as in the main text. (c) The DOS for regular (black line) and amorphous (blue line) lattices for $L_x = 25, L_y = 20, L_z = 44$ with shifting of Landau levels induced by structural disorder indicated by arrows.

For a regular lattice, the Hamiltonian $\hat{H}_T$ describes a Weyl semimetal with double pairs of Weyl points and two pairs of Fermi arcs, as shown schematically in Fig. 5(a). Without magnetic fields, the *anomalous* Hall conductance contributed by each set of Fermi arcs cancels out each other. We thus cannot identify the topological property by probing the anomalous Hall conductance. Fortunately, under magnetic fields along y, the two pairs of Fermi arcs both lead to counterclockwise cyclic motions [see Appendix C], which give rise to nonzero 3D quantum Hall conductance [see the black line in Fig. 5(b) with system size $L_x = 350, L_y = 20$ and $L_z = 40$]. In Fig. 5(b), we also plot the numerically computed Hall conductance with respect to the Fermi energy in amorphous lattices with $L_x = 250, L_y = 20$ and $L_z = 40$ by the blue line, remarkably illustrating the emergence of a quantized plateau at $\overline{\sigma^{\mathrm{H}}_{xy}} = -2e^2/(2h)$ when $E_{\mathrm{F}} \gtrsim 13$. Such a plateau arises from a transition from $\overline{\sigma^{\mathrm{H}}_{xy}} = 0$ to $\overline{\sigma^{\mathrm{H}}_{xy}} = -2e^2/(2h)$ because the two pairs of Fermi arcs in our model are symmetric due to TRS and thus contribute identical Hall conductance.

In addition, we show the bulk-boundary correspondence by calculating the Bott index on amorphous lattices [see the red line in Fig. 5(b) with $L_x = 25, L_y = 20, L_z = 44$], which is consistent with the Hall conductance. Similar to the case without time-reversal symmetry, the shift of the plateau of the Hall conductance in energy is attributed to the right-moving behavior of the Landau levels as shown in Fig. 5(c) for $L_x = 40$, $L_y = 20$ and $L_z = 44$ with arrows indicating the shifting direction of Landau levels induced by structural disorder. Although the Landau levels overlap with each other and renders the system gapless, the bulk states are localized except at a critical point, demonstrated by the normalized localization length $\overline{\Lambda}$ in Fig. 5(d). We see that $\overline{\Lambda}$ decreases as L_x increases far away from $E = 10.7$ and tends to converge to a constant near this energy. The inset shows the result of the finite-size scaling calculations. For $E = 8.1$ and 14, by taking $L_z = 10^4$, we observe a finite slope, indicating the localization behavior, whereas for $E = 10.7$, by taking $L_z = 10^5$, we see a vanishing slope, which is a signature of the critical extended property. Therefore, the quantized Hall conductance arises from the edge states that remain extended; meanwhile, the localized bulk states do not contribute to the transport. The generic mechanism indicates that 3D quantum Hall effect may be broadly used to detect the topology of time-reversal symmetric topological semimetals, provided that the Landau levels are not too close in the energy space.
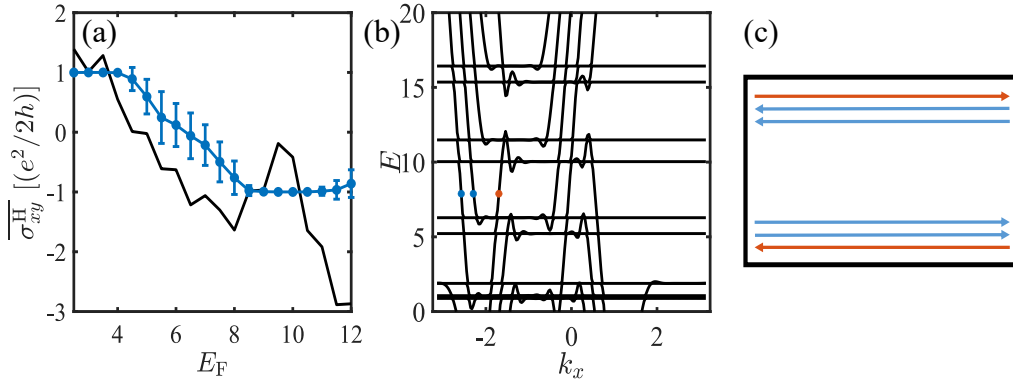
Figure 7: (a) Sample averaged Hall conductance of the time-reversal invariant Hamiltonian (6) under a magnetic field with $B_y = \pi/22$ and $\theta = 10°$. The system size for amorphous lattice (blue line) is $L_x = 250, L_y = 20, L_z = 40$ and for regular lattice (black line) is $L_x = 550, L_y = 20, L_z = 50$. (b) The Landau level spectrum on a regular lattice versus k_x with PBCs in the x direction. Here $L_y = 20$ and $L_z = 60$ with OBCs along both directions. At $E = 8$, the states at one edge are indicated by blue and red points. (c) Schematic of edge states projected onto a single plane with arrows indicating the propagating directions of the electrons.

7 Tilted magnetic field

In this section, we will show that it also occurs under a tilted magnetic field. Specifically, we study the Hamiltonian $\hat{H}$ in the main text under a magnetic field $\boldsymbol{B} = (B_x, B_y, B_z)$ lying in the (y, z) plane with a tilting angle θ from the y axis, i.e. $B_x = 0$ and $B_z = B_y \tan\theta$, as shown in Fig. 6(a). Here, we take $B_y = \pi/22$ and $\theta = 10°$ and the calculated Hall conductance for amorphous (the blue line) and regular (the black line) lattices is displayed in Fig. 6(b). We see that the Hall conductance on amorphous lattices is quantized at $\overline{\sigma_{xy}^{\mathrm{H}}} = -e^2/(2h)$ for $10 \lesssim E_\mathrm{F} \lesssim 13.5$ and at $\overline{\sigma_{xy}^{\mathrm{H}}} = -2e^2/(2h)$ for $15 \lesssim E_\mathrm{F} \lesssim 16$, showing the existence of 3D quantum Hall effect on amorphous lattices. The Hall conductance plateau at a certain value of $\overline{\sigma_{xy}^{\mathrm{H}}}$ moves to higher Fermi energy E_F compared to the Hall conductance on a regular lattice, attributed to the shifting of Landau levels to the higher energy as shown in the DOS in Fig. 6(c) (in amorphous lattices, the Landau levels shift roughly the distance of two Landau levels compared with the regular lattice, indicated by the arrows). We also observe that although the component of the magnetic field perpendicular to the top and bottom surface, namely B_y is the same as in the main text, the Hall conductance is different at the same Fermi energy E_F [compared with the blue line in Fig. 2(a) in the main text], implying the angle dependence of 3D quantum Hall effect on amorphous lattices, similar to the regular case [40]. Note that the Hall conductance is not well quantized at $\overline{\sigma_{xy}^{\mathrm{H}}} = -2e^2/(2h)$ for $10.5 \lesssim E_\mathrm{F} \lesssim 15$ and at $\overline{\sigma_{xy}^{\mathrm{H}}} = -4e^2/(2h)$ for $15.5 \lesssim E_\mathrm{F} \lesssim 16.5$ on the regular lattice due to finite-size effect.

We also study the time-reversal invariant Hamiltonian (6) under a tilted magnetic field with $\theta = 10°$. Surprisingly, on amorphous lattices we see a transition from a plateau of Hall conductance at $\overline{\sigma_{xy}^{\mathrm{H}}} = e^2/(2h)$ to a plateau at $\overline{\sigma_{xy}^{\mathrm{H}}} = -e^2/(2h)$ as shown in Fig. 7 (the blue line), in stark contrast to the case under a vertical magnetic field with Hall conductance quantized at even integer values in units of $e^2/(2h)$, shown in Fig. 5(b). However, on a regular lattice no quantized plateaus of Hall conductance arise in the same energy region up to $L_x = 550$ and no signature of quantization is observed during the increasing of the system size. To elaborate on the reason why quantized Hall conductance emerge on amorphous lattices while is absent on the regular lattice, we show the energy spectrum with respect to the lattice momentum k_x

on a regular lattice in Fig. 7(b), exhibiting Landau levels with edge states going upwards and downwards alternately. For example, within the gap near $E = 8$ (indicated by the blue and red points), there exist two edge states propagating in the same direction (indicated by blue points) and one in opposite direction (indicated by the red point) on each edge, also shown schematically in Fig. 7(c). The quantized Hall conductance is prohibited by the backscattering between the counter-propagating edge states on each edge. On amorphous lattices, a pair of counter-propagating edge states become localized due to disorder with only one edge channel left, resulting in the quantized Hall conductance.

8   Conclusion

In summary, we have theoretically demonstrated the existence of 3D quantum Hall effect in a slab of topological amorphous metals subjected to magnetic fields. We find that while structural disorder significantly broadens the Landau levels such that two neighboring Landau levels overlap with each other, the bulk states are spatially localized except at critical transition energies so that they do not contribute to the Hall conductance. However, due to the topological property of the Landau levels revealed by the Bott index, the edge states arise at distinct hinges on two opposite surfaces, leading to 3D quantum Hall effect. The mechanism of broadening of Landau levels and localization of bulk states is quite generic, independent of the model details. Our results indicate that Weyl band like topology in amorphous materials can be identified through measuring the 3D quantum Hall effect. We also demonstrate the existence of 3D quantum Hall effects in the amorphous system under a tilted magnetic field. Our results suggest that 3D quantum Hall effects may broadly arise in amorphous Weyl like materials. In fact, 3D quantum Hall effect has been experimentally observed in crystalline topological semimetal materials Cd_3As_2 [36–39], which will stimulate further experimental study in broader contexts, including non-crystalline systems. To find concrete material realization of 3D quantum Hall effect in amorphous systems is an important and promising direction for further research. In addition, our results demonstrate the presence of Landau levels in 3D amorphous systems, which may stimulate further investigation into the quantum Hall effect in amorphous topological insulators [72], such as Bi_2Se_3, under magnetic fields.

Acknowledgements

A   Surface spectral function without magnetic fields

In this Appendix, we will calculate the surface spectral function of Hamiltonian (1) under no magnetic field to show ARPES measurement may be difficult for topological amorphous metals.
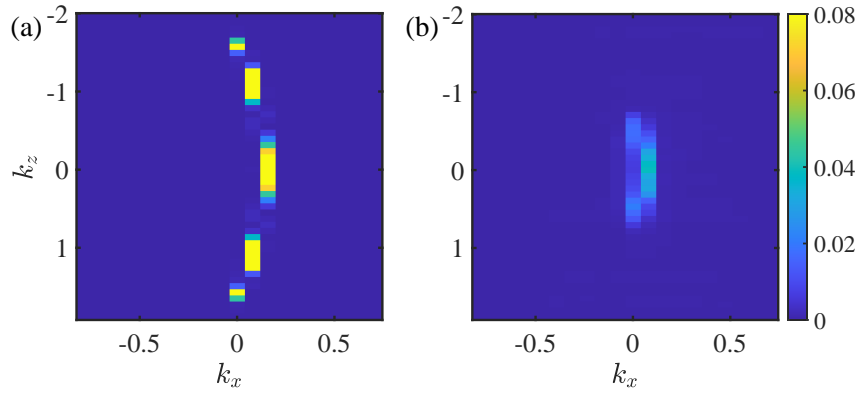
Figure 8: Surface spectral function for the top surface at $E = 9$ on regular (a) and amorphous (b) lattices.

The observable extracted by ARPES is the surface spectral function

$$A(\boldsymbol{k}, E) = \sum_l \langle \boldsymbol{k}, l | \delta(H - E) | \boldsymbol{k}, l \rangle, \tag{7}$$

where $|\boldsymbol{k}, l\rangle$ is the plane wave with wave vector $\boldsymbol{k} = (k_x, k_z)$ restricted in the surface layer in the y direction associated with internal degree of freedom l. Here we take H as the Hamiltonian (1) under no magnetic field and E as the energy of the Weyl point. On the regular lattice, we see a clear Fermi arc on the top surface, as shown in Fig. 8(a). Note that the discontinuity of the Fermi arc is due to the finite size of the system. On the other hand, on amorphous lattices as shown in Fig. 8(b), the signature of the Fermi arc is much more vague, suggesting the difficulty in detecting the topology by ARPES here.

B Explanation of the constraint on the thickness along the y direction

In the main text, we use a slab geometry thin along y for the calculation of the Hall conductance because a finite thickness along y is necessary to the 3D quantum Hall effect even in the crystalline Weyl semimetal. In this Appendix, we will explain the reason in detail.

We show the energy spectrum of Hamiltonian (1) under a magnetic field with $B = \pi/22$ in Fig. 9(a)-(b), with the energy of the Weyl point indicated by the red line. Here we consider a regular lattice with PBCs in both x and z directions. Note that the Landau levels are not perfectly flat due to the lattice effect. We take $L_y = 20$ for Fig. 9(a), $L_y = 60$ for Fig. 9(b) and $L_z = 44$ for both. Obviously, the Landau levels for $L_y = 60$ are much denser than $L_y = 20$, indicating the decrease of separation between Landau levels as the thickness in the y direction increases. We show the energy separation between Landau levels Δ_E as a function of L_y in logarithmic scale in Fig. 9(c), where Δ_E is defined as the magnitude of the energy gap within which the energy of the Weyl point lie at $k_x = 0$. We obtain $\Delta_E \propto L_y^{-0.72}$, indicating that the Landau levels will get closer and closer in the energy space with the increasing of the thickness of the sample and touch each other in the thermodynamic limit, leading to the disappearance of the 3D quantum Hall effect. Therefore, the 3D quantum Hall effect needs a finite thickness along y for a sample even in the crystalline case. Similarly, in the presence of disorder, the Landau levels cannot be too close in energy for the quantum Hall effect, so the sample cannot be too thick.
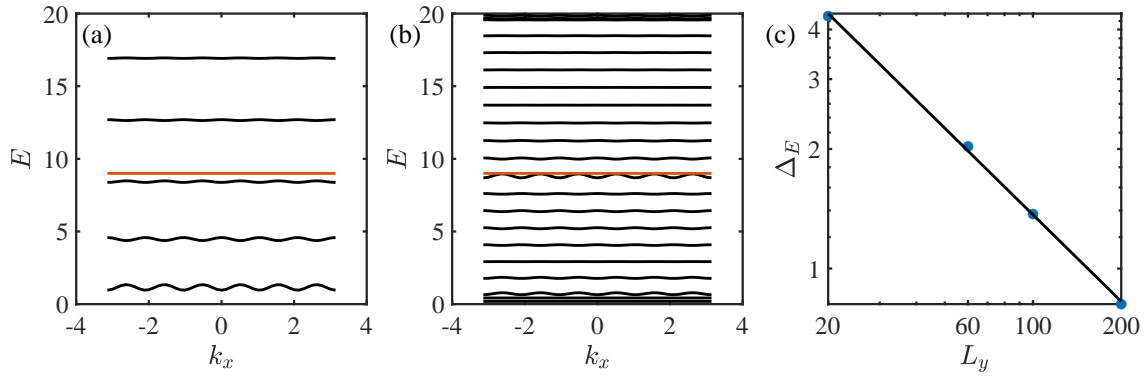
Figure 9: (a)-(b) Landau level spectra of Hamiltonian (1) on a regular lattice under a magnetic field $B = \pi/22$ near the energy of the Weyl point (the red line). $L_y = 20, L_z = 44$ for (a) and $L_y = 60, L_z = 44$ for (b). (c) Finite-size scaling of the energy gap Δ_E with respect to L_y at $L_z = 44$.

C Semiclassical explanation of the 3D quantum Hall effect for a time-reversal invariant Hamiltonian on regular lattices

In the main text, we have shown that 3D quantum Hall effect can arise in a time-reversal invariant Hamiltonian $\hat{H}_T$ with double pairs of Weyl points on regular lattices under a magnetic field. In this Appendix, through semiclassical analysis based on the semiclassical equations of motion [40], we will account for why the two pairs of Fermi arcs give rise to nonzero quantum Hall conductance rather than cancel out the contribution from each other as for the *anomalous* Hall conductivity without magnetic fields.

The double pairs of Weyl points and two loops of Fermi arcs on top and bottom surfaces of the Hamiltonian in a regular lattice are schematically shown in Fig. 10(a). For clarity, we project the Fermi arcs on both surfaces onto the same plane. At Weyl points, Fermi arcs on opposite surfaces are connected by chiral Landau levels. The semiclassical equation of motion $\dot{r} = \partial \varepsilon_k / (\hbar \partial k)$ tells us that the real space velocity $\dot{r}$ is perpendicular to the Fermi arc. In our case, $\dot{r}$ points out of the loops formed by Fermi arcs, as indicated in Fig. 10(a). Under a magnetic field along y, the electronic wave packets cycle along the loops of Fermi arcs counterclockwise in momentum space, also shown in Fig. 10(a), determined by the equation $\hbar \dot{k} = -e\dot{r} \times B$. Specifically, as illustrated in Fig. 10(b), for an electron starting from the Weyl point A_{1m} on the top surface in momentum space, it will move along the Fermi arc to another Weyl point B_{1m} and then tunnel to B'_{1m} on the bottom surface. Later, the electron travels along the Fermi arc on the bottom surface to A'_{1m} and tunnel back to A_{1m}, completing a cyclic motion in momentum space. Correspondingly, in real space, the electron moves from A_{1r} to B_{1r} and then tunnel to B'_{1r} on the bottom surface, as shown in Fig. 10(c). After traveling to A'_{1r} and tunneling back to A_{1r}, a cyclic motion in real space is completed. The cyclic behavior of electrons on the other pair of Fermi arcs [between A_{2m} (A'_{2m}) and B_{2m} (B'_{2m})] and corresponding real space motions can be extracted in a similar manner. Viewed from the positive direction of the y axis, in both momentum and real space, the cyclic directions of electrons dominated by two loops of Fermi arcs are both counterclockwise. In fact, the same cycling direction for different pairs of Fermi arcs is ensured by the time-reversal symmetry. At the edge, the cyclic motions cannot be finished, giving rise to edge states, as shown in Fig. 10(d). The edge states contributed by the left pair of Fermi arcs are indicated by grey color and those contributed by the right pair are colored green. Under the setup of Hall conductance measurement in Fig. 2(b) in the main text, the two pairs of edge states contribute quantum Hall conductance
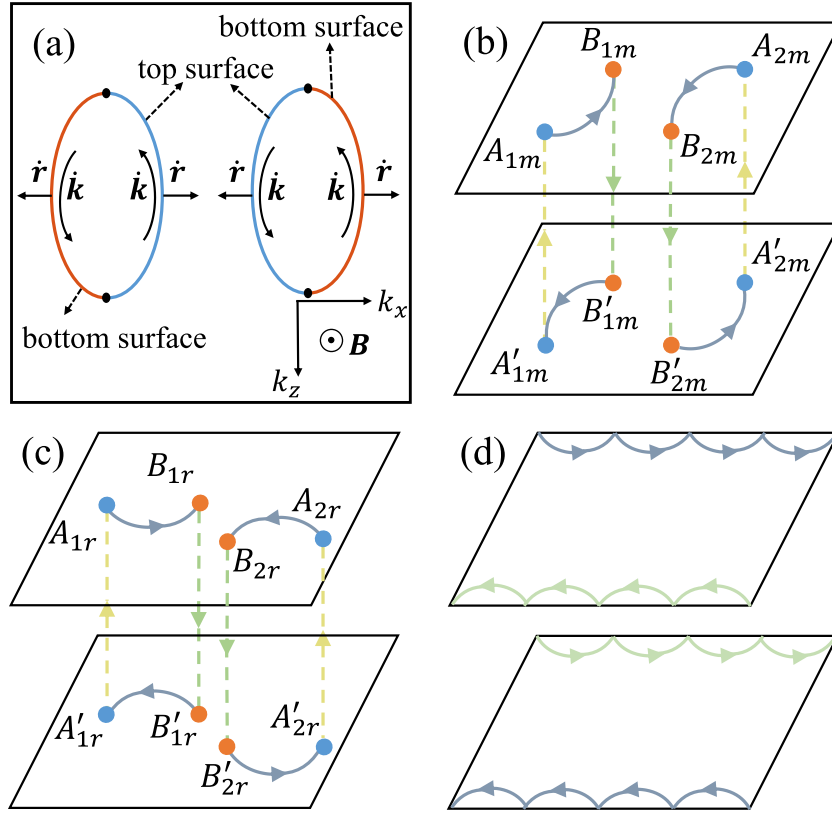
Figure 10: (a) Schematic of Weyl points and Fermi arcs on top and bottom surfaces projected onto a single plane for the Hamiltonian $\hat{H}_T$ on a regular lattice in the main text. The velocities of the center of mass of an electronic wave packet $\dot{k}$ and $\dot{r}$ in momentum and real space, respectively, under a magnetic field in y direction are indicated in the figure. (b) Schematic of cyclic motions of electrons in momentum space where Weyl points are denoted by A_{im} (A'_{im}) and B_{im} (B'_{im}) with $i = 1, 2$. The chiral Landau levels tunneling from top to bottom surface and vise versa are colored green and yellow, respectively. (c) Schematic of cyclic motions of electrons in real space. (d) Schematic of edge states contributed by the left pair (colored grey) and right pair (colored green) of Fermi arcs.

with the same sign and nonzero total quantum Hall conductance is measurable.

References

[1] S. Jia, S.-Y. Xu, and M. Z. Hasan, *Weyl semimetals, Fermi arcs and chiral anomalies*, Nat. Mater. **15**, 1140 (2016), doi:10.1038/nmat4787.

[2] A. A. Burkov, *Topological semimetals*, Nat. Mater. **15**, 1145 (2016), doi:10.1038/nmat4788.

[3] N. P. Armitage, E. J. Mele, and A. Vishwanath, *Weyl and Dirac semimetals in three-dimensional solids*, Rev. Mod. Phys. **90**, 015001 (2018), doi:10.1103/RevModPhys.90.015001.

[4] Y. Xu, *Topological gapless matters in three-dimensional ultracold atomic gases*, Front. Phys. **14**, 43402 (2019), doi:10.1007/s11467-019-0896-1.

[5] B. Q. Lv, T. Qian, and H. Ding, *Experimental perspective on three-dimensional topological semimetals*, Rev. Mod. Phys. **93**, 025002 (2021), doi:10.1103/RevModPhys.93.025002.

[6] X. Wan, A. M. Turner, A. Vishwanath, and S. Y. Savrasov, *Topological semimetal and Fermi-arc surface states in the electronic structure of pyrochlore iridates*, Phys. Rev. B **83**, 205101 (2011), doi:10.1103/PhysRevB.83.205101.

[7] K.-Y. Yang, Y.-M. Lu, and Y. Ran, *Quantum Hall effects in a Weyl semimetal: Possible application in pyrochlore iridates*, Phys. Rev. B **84**, 075129 (2011), doi:10.1103/PhysRevB.84.075129.

[8] A. A. Burkov and L. Balents, *Weyl semimetal in a topological insulator multilayer*, Phys. Rev. Lett. **107**, 127205 (2011), doi:10.1103/PhysRevLett.107.127205.

[9] G. Xu, H. Weng, Z. Wang, X. Dai, and Z. Fang, *Chern semimetal and the quantized anomalous Hall effect in $HgCr_2Se_4$*, Phys. Rev. Lett. **107**, 186806 (2011), doi:10.1103/PhysRevLett.107.186806.

[10] B. Sbierski, G. Pohl, E. J. Bergholtz, and P. W. Brouwer, *Quantum transport of disordered Weyl semimetals at the nodal point*, Phys. Rev. Lett. **113**, 026602 (2014), doi:10.1103/PhysRevLett.113.026602.

[11] A. C. Potter, I. Kimchi, and A. Vishwanath, *Quantum oscillations from surface Fermi arcs in Weyl and Dirac semimetals*, Nat. Commun. **5**, 5161 (2014), doi:10.1038/ncomms6161.

[12] E. J. Bergholtz, Z. Liu, M. Trescher, R. Moessner, and M. Udagawa, *Topology and interactions in a frustrated slab: tuning from Weyl semimetals to $\mathscr{C} > 1$ fractional Chern insulators*, Phys. Rev. Lett. **114**, 016806 (2015), doi:10.1103/PhysRevLett.114.016806.

[13] H. Weng, C. Fang, Z. Fang, B. A. Bernevig, and X. Dai, *Weyl semimetal phase in noncentrosymmetric transition-metal monophosphides*, Phys. Rev. X **5**, 011029 (2015), doi:10.1103/PhysRevX.5.011029.

[14] T. Dubček, C. J. Kennedy, L. Lu, W. Ketterle, M. Soljačić, and H. Buljan, *Weyl points in three-dimensional optical lattices: synthetic magnetic monopoles in momentum space*, Phys. Rev. Lett. **114**, 225301 (2015), doi:10.1103/PhysRevLett.114.225301.

[15] S.-Y. Xu, I. Belopolski, N. Alidoust, M. Neupane, G. Bian, C. Zhang, R. Sankar, G. Chang, Z. Yuan, C.-C. Lee, S.-M. Huang, H. Zheng, J. Ma, D. S. Sanchez, B. Wang, A. Bansil, F. Chou, P. P.Shibayev, H. Lin, S. Jia, and M. Z. Hasan, *Discovery of a Weyl fermion semimetal and topological Fermi arcs*, Science **349**, 613 (2015), doi:10.1126/science.aaa9297.

[16] L. Lu, Z. Wang, D. Ye, L. Ran, L. Fu, J. D. Joannopoulos, and M. Soljačić, *Experimental observation of Weyl points*, Science **349**, 622 (2015), doi:10.1126/science.aaa9273.

[17] B. Q. Lv, H. M. Weng, B. B. Fu, X. P. Wang, H. Miao, J. Ma, P. Richard, X. C. Huang, L. X. Zhao, G. F. Chen, Z. Fang, X. Dai, T. Qian, and H. Ding, *Experimental discovery of Weyl semimetal TaAs*, Phys. Rev. X **5**, 031013 (2015), doi:10.1103/PhysRevX.5.031013.

[18] S. A. Yang, H. Pan, and F. Zhang, *Chirality-dependent Hall effect in Weyl semimetals*, Phys. Rev. Lett. **115**, 156603 (2015), doi:10.1103/PhysRevLett.115.156603.

[19] C.-Z. Chen, J. Song, H. Jiang, Q.-F. Sun, Z. Wang, and X. C. Xie, *Disorder and metal-insulator transitions in Weyl semimetals*, Phys. Rev. Lett. **115**, 246603 (2015), doi:10.1103/PhysRevLett.115.246603.

[20] Y. Xu, F. Zhang, and C. Zhang, *Structured Weyl points in spin-orbit coupled fermionic superfluids*, Phys. Rev. Lett. **115**, 265304 (2015), doi:10.1103/PhysRevLett.115.265304.

[21] A. A. Soluyanov, D. Gresch, Z. Wang, Q. Wu, M. Troyer, X. Dai, and B. A. Bernevig, *Type-II Weyl semimetals*, Nature (London) **527**, 495 (2015), doi:10.1038/nature15768.

[22] Y. Zhang, D. Bulmash, P. Hosur, A. C. Potter, and A. Vishwanath, *Quantum oscillations from generic surface Fermi arcs and bulk chiral modes in Weyl semimetals*, Sci. Rep. **6**, 23741 (2016), doi:10.1038/srep23741.

[23] J. H. Pixley, D. A. Huse, and S. Das Sarma, *Rare-region-induced avoided quantum criticality in disordered three-dimensional Dirac and Weyl semimetals*, Phys. Rev. X **6**, 021042 (2016), doi:10.1103/PhysRevX.6.021042.

[24] L. Huang, T. M. McCormick, M. Ochi, Z. Zhao, M.-T. Suzuki, R. Arita, Y. Wu, D. Mou, H. Cao, J. Yan, N. Trivedi, and A. Kaminski, *Spectroscopic evidence for a type II Weyl semimetallic state in MoTe$_2$*, Nat. Mater. **15**, 1155 (2016), doi:10.1038/nmat4685.

[25] K. Deng, G. Wan, P. Deng, K. Zhang, S. Ding, E. Wang, M. Yan, H. Huang, H. Zhang, Z. Xu, J. Denlinger, A. Fedorov, H. Yang, W. Duan, H. Yao, Y. Wu, S. Fan, H. Zhang, X. Chen, and S. Zhou, *Experimental observation of topological Fermi arcs in type-II Weyl semimetal MoTe$_2$*, Nat. Phys. **12**, 1105 (2016), doi:10.1038/nphys3871.

[26] H. Ishizuka, T. Hayata, M. Ueda, and N. Nagaosa, *Emergent electromagnetic induction and adiabatic charge pumping in noncentrosymmetric Weyl semimetals*, Phys. Rev. Lett. **117**, 216601 (2016), doi:10.1103/PhysRevLett.117.216601.

[27] Y. Xu and L.-M. Duan, *Type-II Weyl points in three-dimensional cold-atom optical lattices*, Phys. Rev. A **94**, 053619 (2016), doi:10.1103/PhysRevA.94.053619.

[28] S. V. Syzranov and L. Radzihovsky, *High-dimensional disorder-driven phenomena in Weyl semimetals, semiconductors, and related systems*, Annu. Rev. Condens. Matter Phys. **9**, 35 (2018), doi:10.1146/annurev-conmatphys-033117-054037.

[29] J. H. Pixley, J. H. Wilson, D. A. Huse, and S. Gopalakrishnan, *Weyl semimetal to metal phase transitions driven by quasiperiodic potentials*, Phys. Rev. Lett. **120**, 207604 (2018), doi:10.1103/PhysRevLett.120.207604.

[30] D. Ma, H. Jiang, H. Liu, and X. C. Xie, *Planar Hall effect in tilted Weyl semimetals*, Phys. Rev. B **99**, 115121 (2019), doi:10.1103/PhysRevB.99.115121.

[31] D. F. Liu, A. J. Liang, E. K. Liu, Q. N. Xu, Y. W. Li, C. Chen, D. Pei, W. J. Shi, S. K. Mo, P. Dudin, T. Kim, C. Cacho, G. Li, Y. Sun, L. X. Yang, Z. K. Liu, S. S. P. Parkin, C. Felser, and Y. L. Chen, *Magnetic Weyl semimetal phase in a kagomé crystal*, Science **365**, 1282 (2019), doi:10.1126/science.aav2873.

[32] N. Morali, R. Batabyal, P. K. Nag, E. Liu, Q. Xu, Y. Sun, B. Yan, C. Felser, N. Avraham, and H. Beidenkopf, *Fermi-arc diversity on surface terminations of the magnetic Weyl semimetal Co$_3$Sn$_2$S$_2$*, Science **365**, 1286 (2019), doi:10.1126/science.aav2334.

[33] Z.-Q. Zhang, B.-L. Wu, C.-Z. Chen, and H. Jiang, *Global phase diagram of disordered higher-order Weyl semimetals*, Phys. Rev. B **104**, 014203 (2021), doi:10.1103/PhysRevB.104.014203.

[34] S. Nandy, C. Lane, and J.-X. Zhu, *Quantum Hall effect in a Weyl-Hubbard model: interplay between topology and correlation*, Phys. Rev. B **109**, 085111 (2024), doi:10.1103/PhysRevB.109.085111.

[35] C.-M. Wang, H.-P. Sun, H.-Z. Lu, and X.-C. Xie, *3D quantum Hall effect of Fermi arcs in topological semimetals*, Phys. Rev. Lett. **119**, 136806 (2017), doi:10.1103/PhysRevLett.119.136806.

[36] C. Zhang, A. Narayan, S. Lu, J. Zhang, H. Zhang, Z. Ni, X. Yuan, Y. Liu, J.-H. Park, E. Zhang, W. Wang, S. Liu, L. Cheng, L. Pi, Z. Sheng, S. Sanvito, and F. Xiu, *Evolution of Weyl orbit and quantum Hall effect in Dirac semimetal Cd_3As_2*, Nat. Commun. **8**, 1272 (2017), doi:10.1038/s41467-017-01438-y.

[37] M. Uchida, Y. Nakazawa, S. Nishihaya, K. Akiba, M. Kriener, Y. Kozuka, A. Miyake, Y. Taguchi, M. Tokunaga, N. Nagaosa, Y. Tokura, and M. Kawasaki, *Quantum Hall states observed in thin films of Dirac semimetal Cd_3As_2*, Nat. Commun. **8**, 2274 (2017), doi:10.1038/s41467-017-02423-1.

[38] T. Schumann, L. Galletti, D. A. Kealhofer, H. Kim, M. Goyal, and S. Stemmer, *Observation of the quantum Hall effect in confined films of the three-dimensional Dirac semimetal Cd_3As_2*, Phys. Rev. Lett. **120**, 016801 (2018), doi:10.1103/PhysRevLett.120.016801.

[39] C. Zhang, Y. Zhang, X. Yuan, S. Lu, J. Zhang, A. Narayan, Y. Liu, H. Zhang, Z. Ni, R. Liu, E. S. Choi, A. Suslov, S. Sanvito, L. Pi, H.-Z. Lu, A. C. Potter, and F. Xiu, *Quantum Hall effect based on Weyl orbit in Cd_3As_2*, Nature (London) **565**, 331 (2019), doi:10.1038/s41586-018-0798-3.

[40] H.-L. Li, H.-W. Liu, H. Jiang, and X.-C. Xie, *3D quantum Hall effect and a global picture of edge states in Weyl semimetals*, Phys. Rev. Lett. **125**, 036602 (2020), doi:10.1103/PhysRevLett.125.036602.

[41] C. Zhang, Y. Zhang, H.-Z. Lu, X. C. Xie, and F. Xiu, *Cycling Fermi arc electrons with Weyl orbits*, Nat. Rev. Phys. **3**, 660 (2021), doi:10.1038/s42254-021-00344-z.

[42] R. Chen, T. Liu, C. M. Wang, H.-Z. Lu, and X. C. Xie, *Field-tunable one-sided higher-order topological hinge states in Dirac semimetals*, Phys. Rev. Lett. **127**, 066801 (2021), doi:10.1103/PhysRevLett.127.066801.

[43] S. Li, C. M. Wang, Z. Z. Du, F. Qin, H.-Z. Lu, and X. C. Xie, *3D quantum Hall effects and nonlinear Hall effect*, npj Quantum Mater. **6**, 96 (2021), doi:10.1038/s41535-021-00399-2.

[44] M. Chang, Y. Ge, and L. Sheng, *Generalization of the theory of three-dimensional quantum Hall effect of Fermi arcs in Weyl semimetal*, Chin. Phys. B **31**, 057304 (2022), doi:10.1088/1674-1056/ac5c32.

[45] F. Xiong, C. Honerkamp, D. M. Kennes, and T. Nag, *Understanding the three-dimensional quantum Hall effect in generic multi-Weyl semimetals*, Phys. Rev. B **106**, 045424 (2022), doi:10.1103/PhysRevB.106.045424.

[46] J.-H. Wang, Y.-B. Yang, and Y. Xu, *Fractional quantum Hall effect based on Weyl orbits*, Phys. Rev. B **111**, 045108 (2025), doi:10.1103/PhysRevB.111.045108.

[47] J.-H. Wang, and Y. Xu, *Transitions from Composite Fermi Liquid to Moore-Read States in Weyl Semimetals*, https://arxiv.org/pdf/2501.03498.

[48] R. Zallen, *The Physics of Amorphous Solids* (A Wiley-Interscience Publication, New York, USA, 1998), doi:10.1002/9783527617968.

[49] A. Agarwala and V. B. Shenoy, *Topological insulators in amorphous systems*, Phys. Rev. Lett. **118**, 236402 (2017), doi:10.1103/PhysRevLett.118.236402.

[50] S. Mansha and Y. D. Chong, *Robust edge states in amorphous gyromagnetic photonic lattices*, Phys. Rev. B **96**, 121405(R) (2017), doi:10.1103/PhysRevB.96.121405.

[51] N. P. Mitchell, L. M. Nash, D. Hexner, A. M. Turner, and W. T. Irvine, *Amorphous topological insulators constructed from random point sets*, Nat. Phys. **14**, 380 (2018), doi:10.1038/s41567-017-0024-5.

[52] C. Bourne and E. Prodan, *Non-commutative Chern numbers for generic aperiodic discrete systems*, J. Phys. A **51**, 235202 (2018), doi:10.1088/1751-8121/aac093.

[53] K. Pöyhönen, I. Sahlberg, A. Weststr̈om, and T. Ojanen, *Amorphous topological superconductivity in a Shiba glass*, Nat. Commun. **9**, 2103 (2018), doi:10.1038/s41467-018-04532-x.

[54] B. Yang, H. Zhang, T. Wu, R. Dong, X. Yan, and X. Zhang, *Topological states in amorphous magnetic photonic lattices*, Phys. Rev. B **99**, 045307 (2019), doi:10.1103/PhysRevB.99.045307.

[55] G. W. Chern, *Topological insulator in an atomic liquid*, Europhys. Lett. **126**, 37002 (2019), doi:10.1209/0295-5075/126/37002.

[56] Y.-B. Yang, T. Qin, D.-L. Deng, L.-M. Duan, and Y. Xu, *Topological amorphous metals*, Phys. Rev. Lett. **123**, 076401 (2019), doi:10.1103/PhysRevLett.123.076401.

[57] M. Costa, G. R. Schleder, M. Buongiorno Nardelli, C. Lewenkopf, and A. Fazzio, *Toward realistic amorphous topological insulators*, Nano Lett. **19**, 8941 (2019), doi:10.1021/acs.nanolett.9b03881.

[58] I. Sahlberg, A. Weststr̈om, K. Pöyhönen, and T. Ojanen, *Topological phase transitions in glassy quantum matter*, Phys. Rev. Research **2**, 013053 (2020), doi:10.1103/PhysRevResearch.2.013053.

[59] P. Mukati, A. Agarwala, and S. Bhattacharjee, *Topological and conventional phases of a three-dimensional electronic glass*, Phys. Rev. B **101**, 035142 (2020), doi:10.1103/PhysRevB.101.035142.

[60] A. Agarwala, V. Juričić, and B. Roy, *Higher-order topological insulators in amorphous solids*, Phys. Rev. Research **2**, 012067(R) (2020), doi:10.1103/PhysRevResearch.2.012067.

[61] H. Huang and F. Liu, *A unified view of topological phase transition in band theory*, Research **2020**, 7832610 (2020), doi:10.34133/2020/7832610.

[62] P. Zhou, G.-G. Liu, X. Ren, Y. Yang, H. Xue, L. Bi, L. Deng, Y. Chong, and B. Zhang, *Photonic amorphous topological insulator*, Light Sci. Appl. **9**, 133 (2020), doi:10.1038/s41377-020-00368-7.

[63] Q. Marsal, D. Varjas, and A. G. Grushin, *Topological Weaire-Thorpe models of amorphous matter*, Proc. Natl. Acad. Sci. U.S.A. **117**, 30260 (2020), doi:10.1073/pnas.2007384117.

[64] M. N. Ivaki, I. Sahlberg, and T. Ojanen, *Criticality in amorphous topological matter: Beyond the universal scaling paradigm*, Phys. Rev. Research **2**, 043301 (2020), doi:10.1103/PhysRevResearch.2.043301.

[65] B. Focassio, G. R. Schleder, M. Costa, A. Fazzio, and C. Lewenkopf, *Structural and electronic properties of realistic two-dimensional amorphous topological insulators*, 2D Mater. **8**, 025032 (2021), doi:10.1088/2053-1583/abdb97.

[66] J.-H. Wang, Y.-B. Yang, N. Dai, and Y. Xu, *Structural-disorder-induced second-order topological insulators in three dimensions*, Phys. Rev. Lett. **126**, 206404 (2021), doi:10.1103/PhysRevLett.126.206404.

[67] K. Li, J.-H. Wang, Y.-B. Yang, and Y. Xu, *Symmetry-protected topological phases in a Rydberg glass*, Phys. Rev. Lett. **127**, 263004 (2021), doi:10.1103/PhysRevLett.127.263004.

[68] C. Wang, T. Cheng, Z. Liu, F. Liu, and H. Huang, *Structural amorphization-induced topological order*, Phys. Rev. Lett. **128**, 056401 (2022), doi:10.1103/PhysRevLett.128.056401.

[69] A. G. Grushin, *Topological phases of amorphous matter*, in *Low-Temperature Thermal and Vibrational Properties of Disordered Solids*, edited by M. A. Ramos (World Scientific, Singapore, 2022), Chap. 11, doi:10.1142/9781800612587_0011.

[70] J. D. Hannukainen, M. F. Martínez, J. H. Bardarson, and T. K. Kvorning, *Local topological markers in odd spatial dimensions and their application to amorphous topological matter*, Phys. Rev. Lett. **129**, 277601 (2022), doi:10.1103/PhysRevLett.129.277601.

[71] S. Kim, A. Agarwala, and D. Chowdhury, *Fractionalization and topology in amorphous electronic solids*, Phys. Rev. Lett. **130**, 026202 (2023), doi:10.1103/PhysRevLett.130.026202.

[72] P. Corbae, S. Ciocys, D. Varjas, S. Zeltmann, C. H. Stansbury, M. Molina-Ruiz, S. Griffin, C. Jozwiak, Z. Chen, L.-W. Wang, A. M. Minor, A. G. Grushin, A. Lanzara, and F. Hellman, *Observation of spin-momentum locked surface states in amorphous Bi_2Se_3*, Nat. Mater. **22**, 200 (2023), doi:10.1038/s41563-022-01458-0.

[73] I. Sahlberg, M. N. Ivaki, K. Pöyhönen, and T. Ojanen, *Quantum Hall effect and Landau levels without spatial long-range correlations*, Phys. Rev. Research **5**, 033218 (2023), doi:10.1103/PhysRevResearch.5.033218.

[74] Z. Zhang, P. Delplace, and R. Fleury, *Anomalous topological waves in strongly amorphous scattering networks*, Sci. Adv. **9**, eadg3186 (2023), doi:10.1126/sciadv.adg3186.

[75] P. Corbae, J. D. Hannukainen, Q. Marsal, D. Muñoz-Segovia, and A. G. Grushin, *Amorphous topological matter: Theory and experiment*, Europhys. Lett. **142**, 16001 (2023), doi:10.1209/0295-5075/acc2e2.

[76] Y.-L. Tao, J.-H. Wang, and Y. Xu, *Average symmetry protected higher-order topological amorphous insulators*, SciPost Phys. **15**, 193 (2023), doi:10.21468/SciPostPhys.15.5.193.

[77] Y.-B. Yang, J.-H. Wang, K. Li, and Y. Xu, *Higher-order topological phases in crystalline and non-crystalline systems: a review*, J. Phys.: Condens. Matter **36**, 283002 (2024), doi:10.1088/1361-648X/ad3abd.

[78] H. Schulz-Baldes, and T. Stoiber, *Invariants of disordered semimetals via the spectral localizer*, Europhys. Lett. **136**, 27001 (2022), doi:10.1209/0295-5075/ac1b65.

[79] A. Cerjan and T. A. Loring, *Local invariants identify topology in metals and gapless systems*, Phys. Rev. B **106**, 064109 (2022), doi:10.1103/PhysRevB.106.064109.

[80] H. Schulz-Baldes, and T. Stoiber, *Spectral localization for semimetals and Callias operators*, J. Math. Phys. **64**,081901 (2023), doi:10.1063/5.0093983.

[81] K. Y. Dixon, T. A. Loring, and A. Cerjan, *Classifying Topology in Photonic Heterostructures with Gapless Environments*, Phys. Rev. Lett. **131**, 213801 (2023), doi:10.1103/PhysRevLett.131.213801.

[82] S. Franca, and A. G. Grushin, *Topological diffusive metal in amorphous transition metal monosilicides*, Phys. Rev. Materials **8**, L021201 (2024), doi:10.1103/PhysRevMaterials.8.L021201.

[83] L. Schweitzer, B. Kramer, and A. MacKinnon, *The conductivity of a two-dimensional electronic system of finite width in the presence of a strong perpendicular magnetic field and a random potential*, Z. Phys. B **59**, 379 (1985), doi:10.1007/BF01328845.

[84] A. MacKinnon, *The calculation of transport properties and density of states of disordered solids*, Z. Phys. B **59**, 385 (1985), doi:10.1007/BF01328846.

[85] S. Datta, *Electronic Transport in Mesoscopic Systems* (Cambridge University Press, Cambridge, UK, 1997), doi:10.1017/CBO9780511805776.

[86] Y. Xing, Q.-F. Sun, and J. Wang, *Symmetry and transport property of spin current induced spin-Hall effect*, Phys. Rev. B **75**, 075324 (2007), doi:10.1103/PhysRevB.75.075324.

[87] M. B. Hastings and T. A. Loring, *Almost commuting matrices, localized Wannier functions, and the quantum Hall effect*, J. Math. Phys. **51**, 015214 (2010), doi:10.1063/1.3274817.

[88] T. A. Loring and M. B. Hastings, *Disordered topological insulators via C^*-algebras*, Europhys. Lett. **92**, 67004 (2010), doi:10.1209/0295-5075/92/67004.

[89] D. Xiao, M.-C. Chang, and Q. Niu, *Berry phase effects on electronic properties*, Rev. Mod. Phys. **82**, 1959 (2010), doi:10.1103/RevModPhys.82.1959.

[90] A. Weiße, G. Wellein, A. Alvermann, and H. Fehske, *The kernel polynomial method*, Rev. Mod. Phys. **78**, 275 (2006), doi:10.1103/RevModPhys.78.275.

[91] A. MacKinnon and B. Kramer, *One-parameter scaling of localization length and conductance in disordered systems*, Phys. Rev. Lett. **47**, 1546 (1981), doi:10.1103/PhysRevLett.47.1546.

[92] A. MacKinnon and B. Kramer, *The scaling theory of electrons in disordered solids: Additional numerical results*, Z. Phys. B **53** 1 (1983), doi:10.1007/BF01578242.